Research Article Vol. 4, No. 4 / April 2017 / Optica 412

Non-equilibrium ultrashort pulse generation strategies in VECSELs

I. Kilen,[1,*] S. W. Koch,[2,3] J. Hader,[2,4] and J. V. Moloney[1,2,4,5]

[1]Program in Applied Mathematics, University of Arizona, Tucson, Arizona 85721, USA
[2]College of Optical Sciences, University of Arizona, 1630 East University Boulevard, Tucson, Arizona 85721, USA
[3]Department of Physics and Material Sciences Center, Philipps-Universität Marburg, Renthof 5, 35032 Marburg, Germany
[4]Nonlinear Control Strategies Inc., Tucson, Arizona 85704, USA
[5]Department of Mathematics, University of Arizona, 617 N. Santa Rita Ave., Tucson, Arizona 85721, USA
*Corresponding author: ikilen@math.arizona.edu

Received 14 December 2016; revised 27 February 2017; accepted 28 February 2017 (Doc. ID 282630); published 27 March 2017

Vertical external cavity surface emitting lasers are ideal testbeds for studying nonlinear many-body systems driven far from equilibrium. The classical laser gain picture fails, however, when a high peak intensity optical pulse of duration shorter than the intrinsic carrier scattering time interacts with electrons in the conduction and holes in the valence band, and the non-equilibrium carrier distributions cannot recover during the presence of the exciting pulse. We present the optimization of ultrashort mode-locked pulses in a vertical external cavity surface emitting laser cavity with a saturable absorber mirror by modelling non-equilibrium quantum dynamics of the electron-hole excitations in the semiconductor quantum-well gain and absorber medium via the semiconductor Bloch equations and treating the field propagation at the level of Maxwell's wave equation. We introduce a systematic design that predicts the generation of stable mode-locked pulses of duration less than twenty femtoseconds. This factor of five improvement is of interest for mode-locking and ultrafast semiconductor dynamics applications.

OCIS codes: (140.3430) Laser theory; (140.4050) Mode-locked lasers; (140.5960) Semiconductor lasers; (140.7090) Ultrafast lasers; (140.7270) Vertical emitting lasers.

https://doi.org/10.1364/OPTICA.4.000412

1. INTRODUCTION

The wavelength flexible vertical external-cavity surface-emitting laser (VECSEL) has been a popular subject in recent research [1–15]. Two main applications have been continuous-wave (CW) operation and mode-locked pulse generation. CW lasers have been optimized for maximal output power. So far, up to 106 W has been reached using multimode operation [6,7] and 15 W in single frequency operation [14]. At the same time, stable mode-locked pulses have been found using semiconductor external saturable absorber mirrors (SESAMs) [1,2,4,8,9], graphene and carbon nanotube saturable absorbers [10–12], and integrated quantum well (QW) and quantum dot saturable absorbers [10]. Today, the shortest experimentally realized pulse widths are on the order of 100 fs [3,13,15]. Among these is a train of 60 fs pulses under a picosecond envelope [3] and single 107 fs pulses that were externally compressed down to 96 fs [15].

Given the complexity of the VECSEL system and the wide range of material and design choices, one clearly needs a predictive way to describe the entire mode-locking configuration to reach the shortest possible pulses. For such a quantitative numerical model, one has to consider the microscopic dynamics of the electron-hole excitations in the gain and absorber medium as well as the pulse propagation effects in the entire cavity.

To reduce the numerical complexity, simple models have been used in the past. In particular, a rate-equation type approach that corresponds to an adiabatic eliminating of the microscopic QW polarizations has become popular [16]. One has to fit about a dozen parameters to reproduce experimental observations with such a model. Typically, these parameters are integrated quantities that do not consider the complex microscopic QW dynamics that drive the formation of mode-locked pulses. To utilize these models under different conditions, one needs an ever growing number of fit parameters, and the results are highly sensitive to parameters that are not accurately measurable [15].

To eliminate most of the empirical fitting, in this paper, we use numerical solutions of the Maxwell-semiconductor Bloch equations [17] to treat the light-matter interaction within the QWs. Simulations on the level of second Born–Markov are used to determine coefficients for the higher order correlation effects, such as the polarization dephasing, carrier-carrier scattering, and carrier relaxation. These approximations are convenient because these computations are very time consuming, and previous work has shown that the properties of very short mode-locked pulses are not too strongly influenced by the details of the carrier-carrier scattering dynamics, as long as one uses the consistently determined microscopic values [18].

In high-power applications of VECSELs, one has reached the above mentioned record values by employing so-called resonant periodic gain (RPG) structures [6,7]. Here, the QWs are placed on the antinodes of the standing wave at the desired wavelength to realize maximum light amplification for that particular wavelength. However, such RPG structures are not optimized for ultrashort pulse generation, since this requires optimal amplification of a relatively broad wavelength spectrum. In fact, the shortest experimentally verified mode-locked single pulse results have been obtained with structures that deviate from the RPG design [13,15].

In this paper, we investigate mode locking in VECSEL systems with non-RPG configurations of the gain structure with the goal of finding designs that enable stable ultrashort pulse generation. We demonstrate how the detailed understanding of the microscopic dynamics of the VECSEL structures can be systematically utilized for the system optimization. In the following Section 2, we summarize the main ingredients of our microscopic model before we show examples of our numerical results and discuss the optimization strategy in Section 3. As an idealized example, we present a structure capable of producing stable 19 fs pulses. We conclude this paper by a brief summary in Section 4.

2. MICROSCOPIC THEORY

The systematic numerical simulation of mode-locked VECSELs requires a model for both the electromagnetic field propagating in the cavity as well as the light-matter interaction in optically active QWs. In our approach, the dynamics of the light field in the cavity are modeled by Maxwell's equations. For a light field $E(z,t)$ propagating in the z-direction that is perpendicular to the QW planes, we obtain

$$\left[\frac{\partial^2}{\partial z^2}-\frac{n^2}{c_0^2}\frac{\partial^2}{\partial t^2}\right]E(z,t)=\mu_0\frac{\partial^2}{\partial t^2}P(z,t). \tag{1}$$

Here, c_0 is the speed of light in vacuum, n is the background refractive index of the medium, and μ_0 is the vacuum permeability. The macroscopic optical polarization $P(z,t)$ couples the light field to the microscopic many-body dynamics in the QWs. For a given cavity configuration, the light field will propagate through layers of different materials with the individual value of the background refractive index. At every material interface this causes reflection and phase changes in $E(z,t)$, depending on the specific materials used. Furthermore, when $E(z,t)$ interacts with the QWs, it experiences either absorption or optical gain, depending on the carrier density realized in the respective QW.

The multiband semiconductor Bloch equations (SBE) model the microscopic dynamics in the QWs [17] and enable us to determine the macroscopic optical polarization through $P(z,t)=\sum_{\lambda,\nu,\mathbf{k}}p_{\lambda,\nu,\mathbf{k}}$. The dynamics of the microscopic polarization $p_{\lambda,\nu,\mathbf{k}}$ with crystal momentum $\mathbf{k}$ in the plane of the QW is given by

$$\begin{aligned}\frac{\partial}{\partial t}p_{\lambda,\nu,\mathbf{k}}&=-\frac{\mathrm{i}}{\hbar}\sum_{\lambda_1,\nu_1}(e^{\mathrm{e}}_{\lambda,\lambda_1,\mathbf{k}}\delta_{\nu,\nu_1}+e^{\mathrm{h}}_{\nu,\nu_1,\mathbf{k}}\delta_{\lambda,\lambda_1})p_{\lambda_1,\nu_1,\mathbf{k}}\\&\quad-\mathrm{i}(n^{\mathrm{e}}_{\lambda,\mathbf{k}}+n^{\mathrm{h}}_{\nu,\mathbf{k}}-1)\Omega_{\lambda,\nu,\mathbf{k}}+\Gamma_{\lambda,\nu,\mathrm{deph}},\\\frac{\partial}{\partial t}n^{\mathrm{e(h)}}_{\lambda(\nu),\mathbf{k}}&=-2\,\mathrm{Im}(\Omega_{\lambda,\nu,\mathbf{k}}(p_{\lambda,\nu,\mathbf{k}})^*)+\Gamma^{\mathrm{e(h)}}_{\lambda(\nu),\mathrm{scatt}}+\Gamma^{\mathrm{e(h)}}_{\lambda(\nu),\mathrm{fill}}.\end{aligned} \tag{2}$$

Here, $n^{\mathrm{e(h)}}_{\lambda(\nu),\mathbf{k}}$ is the carrier occupation number at the momentum $\mathbf{k}$ of the electrons (holes) in the conduction (valence) band indicated by $\lambda(\nu)$. The Hartree–Fock renormalized single particle energies are

$$\begin{aligned}e^{\mathrm{e}}_{\lambda,\lambda_1,\mathbf{k}}&=\epsilon^{\mathrm{e}}_{\lambda,\mathbf{k}}\delta_{\lambda,\lambda_1}-\sum_{\lambda_2,\mathbf{q}}V^{\lambda,\lambda_2,\lambda_1,\lambda_2}_{|\mathbf{k}-\mathbf{q}|}n^{\mathrm{e}}_{\lambda_2,\mathbf{q}},\\e^{\mathrm{h}}_{\nu,\nu_1,\mathbf{k}}&=\epsilon^{\mathrm{h}}_{\nu,\mathbf{k}}\delta_{\nu,\nu_1}-\sum_{\nu_2,\mathbf{q}}V^{\nu,\nu_2,\nu_1,\nu_2}_{|\mathbf{k}-\mathbf{q}|}n^{\mathrm{h}}_{\nu_2,\mathbf{q}}\end{aligned} \tag{3}$$

and the corresponding effective Rabi frequency $\Omega_{\lambda,\nu,\mathbf{k}}$ is

$$\hbar\Omega_{\lambda,\nu,\mathbf{k}}=d^{\lambda,\nu}_{\mathbf{k}}E(z,t)+\sum_{\lambda_1,\nu_1,\mathbf{q}\neq\mathbf{k}}V^{\lambda,\nu_1,\nu,\lambda_1}_{|\mathbf{k}-\mathbf{q}|}p_{\lambda_1,\nu_1,\mathbf{q}}, \tag{4}$$

where $V^{\lambda,\nu_1,\nu,\lambda_1}_{|\mathbf{k}-\mathbf{q}|}$ is the Coulomb potential and $d^{\lambda,\nu}_{\mathbf{k}}$ is the dipole matrix element. In Eq. (2), the higher order correlation contributions lead to dephasing of the polarization ($\Gamma_{\lambda,\nu,\mathrm{deph}}$), the carrier scattering ($\Gamma^{\mathrm{e(h)}}_{\lambda(\nu),\mathrm{scatt}}$), the kinetic hole filling ($\Gamma^{\mathrm{e(h)}}_{\lambda(\nu),\mathrm{fill}}$), and the Coulomb screening. To simplify the microscopic model, we only consider QW structures that provide a strong confinement for the electrons and holes. The transition energy for such a two-band structure under the effective mass approximation is given by $\hbar\omega_{\mathbf{k}}=E_{\mathrm{g}}+\frac{\hbar^2\mathbf{k}^2}{2m_{\mathrm{e}}}+\frac{\hbar^2\mathbf{k}^2}{2m_{\mathrm{h}}}$, where E_{g} is the band gap and $m_{\mathrm{e(h)}}$ denotes the effective electron (hole) mass.

To determine the correlation contributions, one has to solve the full many-body problem, for example, on the level of a second-order Born–Markov approximation [19]. For any systematic optimization study of VECSEL mode locking, this is not practical because of the computational cost involved in solving the full equations over many thousands of field round trips in the respective cavities. However, under the experimentally realized conditions of high carrier densities in the semiconductor gain medium, the relatively small changes in total carrier density during mode-locked operation, and, in particular, for ultrashort pulses in the regime below hundreds of femtoseconds, it is possible to make an excellent effective relaxation approximation to the correlation contributions where the effective timescales are extracted from the full microscopic simulation. This simplification reduces the required CPU time to attain a stable mode-locked pulse from months to days.

In our approach, the pump injection is modeled through a relaxation toward a background Fermi distribution $f^{\mathrm{e(h)}}_{\lambda(\nu),\mathbf{k}}$ at the lattice temperature with the carrier scattering $\Gamma^{\mathrm{e(h)}}_{\lambda(\nu),\mathrm{scatt}}=-(n^{\mathrm{e(h)}}_{\lambda(\nu),\mathbf{k}}-f^{\mathrm{e(h)}}_{\lambda(\nu),\mathbf{k}})/\tau_{\mathrm{scatt}}$, the dephasing of the polarization modeled using $\Gamma_{\lambda,\nu,\mathrm{deph}}=-(1/\tau_{\mathrm{deph}})p_{\lambda,\nu,\mathbf{k}}$, and the kinetic hole filling using $\Gamma^{\mathrm{e(h)}}_{\lambda(\nu),\mathrm{fill}}=-(n^{\mathrm{e(h)}}_{\lambda(\nu),\mathbf{k}}-F^{\mathrm{e(h)}}_{\lambda(\nu),\mathbf{k}})/\tau_{\mathrm{fill}}$. τ_{scatt}, τ_{deph}, and τ_{fill} are the effective rates for the respective processes, and the instantaneous quasi-equilibrium Fermi distribution, $F^{\mathrm{e(h)}}_{\lambda(\nu),\mathbf{k}}$, is calculated from the dynamic electron (hole) temperature and density. The kinetic hole filling model reproduces the carrier scattering of the full microscopic calculation while preserving total carrier density and temperature. In this process, carriers at high momentum states scatter down into available lower momentum states; this process results in the filling of kinetic holes in the carrier distributions. With realistic values for τ_{fill}, the dynamic carrier occupation numbers will first relax to $F^{\mathrm{e(h)}}_{\lambda(\nu),\mathbf{k}}$ and then relax back to the background Fermi distribution $f^{\mathrm{e(h)}}_{\lambda(\nu),\mathbf{k}}$.

For detailed understanding of the semiconductor QW interaction dynamics with the ultrashort pulses, the inversion $n^{\mathrm{e}}_{\lambda,\mathbf{k}}(t)+n^{\mathrm{h}}_{\nu,\mathbf{k}}(t)-1$ is the central quantity. If the inversion is positive for some momentum values, the QW will provide optical

gain for the corresponding frequency values and conversely, a negative inversion will result in absorption of those frequencies. When the inversion is reduced to zero, there is neither gain nor absorption at the corresponding frequencies, and we denote this as *bleaching* the inversion at these frequencies.

The spectral range of positive inversion provides the ultimate limit for the spectral width of the amplified pulse and thus, its duration. In addition, the detailed shape of the time dependent inversion is critical in the formation of the pulse and determines what type of pulse, that is, a single pulse, a "pulse molecule," or multiple pulses, will appear as a mode-locked solution [18,20]. For a relatively low level of QW inversion, the resulting intracavity field never becomes strong enough to bleach the inversion, and in this case, the mode-locked solution is a single pulse. For a higher inversion, the intracavity field can increase to a level where it bleaches the inversion in the spectral range around the pulse maximum. Transiently, the QWs can even become absorbing at the corresponding momentum values due to Rabi flopping. The pulse spectrum will in turn split into two separate peaks to more efficiently take advantage of the inverted carriers around the absorbing region. The pulse shape that results from this double peaked spectrum is the "pulse molecule," which has multiple short pulses underneath a much longer envelope in the time domain. Finally, if the inversion is at an even higher level, there are too many carriers in the QWs for only one pulse to exist in the cavity and, to take advantage of this, multiple pulses will appear.

In a VECSEL cavity with a SESAM, the properties of the resulting mode-locked pulse are also influenced by the saturable losses from the SESAM and any other unsaturable losses, such as output coupling [21]. In Ref. [18], we have investigated mode-locking properties as a function of the ratio R_α of saturable absorption in the SESAM to the total cavity loss. R_α has been found to influence the stability of the pulse, the type of pulse, the peak intensity, and the full width at half maximum (FWHM) of the resulting mode-locked pulse. If one systematically wants to determine the optimal value for R_α, one needs to examine the full mode-locking dynamics for a wide range values of the saturable and unsaturable losses. This is a major computational problem that requires a large CPU time investment; however, as a rule of thumb, we found that a high R_α is favorable for ultrashort pulse generation.

As yet another important aspect, one has to be able to manage the cavity group delay dispersion (GDD) to generate ultrashort pulses [5,15,16,22]. When a pulse is propagating through a dispersive media, the group velocity will be frequency dependent, and consequently, different frequency components of the pulse will travel at separate velocities. This will cause the pulse to elongate and, thus, an ideal configuration is designed such that the GDD is minimized in a wide spectral range to produce ultrashort pulses [16,22]. The total GDD in a gain structure is comprised of the dispersion from the material layers as well as the electronic contribution from the active QWs. One can verify that an anti resonant gain region will provide the flattest possible GDD [5]. When growing the material layers in the gain structure, even a 1% deviation of layer thickness can be highly disruptive to the GDD and, according to simulations, when generating ultrashort pulses, a variation of as little as ± 100 fs^2 can result in more than double the pulse length [15].

Clearly, a trivial limitation on ultrashort pulse generation is provided by the spectral width of the distributed Bragg reflector (DBR) stop band. However, the effective spectral pulse width is even smaller because around the stopband edges, the DBR also provides considerable dispersion. For example, the theoretical limit to the width of a DBR stopband centered at 980 nm and composed of AlAs/AlGaAs with refractive indices 2.946 and 3.435 is about 96 nm [23]. A wider DBR stopband can be achieved by using dielectric materials such as Nb_2O_5/SiO_2 with refractive indices 2.26/1.451 and a theoretical limit to the width of about 280 nm, for operation at 980 nm.

3. NUMERICAL RESULTS

In our numerical simulations, the computational domain is modeled as a linear VECSEL cavity and includes a gain chip, an air gap, a SESAM, and an output coupler. The gain chip is built with ten 8-nm InGaAs QWs on top of a DBR. The QWs are arranged as a multiple QW (MQW) structure inside a single antinode, as seen in Fig. 1. Furthermore, we include a cap layer and a single layer of dispersion compensating antireflection (AR) coating. To get an output close to 980 nm the peak gain, DBR and AR coatings are all centered at this wavelength. The QWs are placed symmetrically around the peak of the antinode. Assuming 2-nm barriers enables the placement of ten QWs under the first antinode. This number of wells and spacing was found to yield optimal amounts of gain and field-well coupling. It has been verified that the results do not change significantly if the combination of well and barrier width is changed while leaving the total width at 10 nm. To model the SESAM, we place a single 8-nm InGaAs QW on top of the output coupling mirror with a single layer of AR coating, such as in [18]. The intracavity field has a ten times higher intensity focus on the SESAM compared to the gain chip.

In several of our studies, we use a DBR with a very wide stop band to identify the optimized short-pulse generation conditions without being limited by the spectral DBR width. For this purpose, we use 30 alternating layer pairs of material with refractive indices of 1.9 and 3.435 to obtain a theoretical stopband width of 377 nm. While this change is made for simplicity, a wider stopband could also have resulted from using a dielectric DBR. We compare the optimized results for this configuration with those obtained for a GaAs/AlGaAs DBR with 30 repeats and a theoretical limit to the stopband width of about 96 nm.

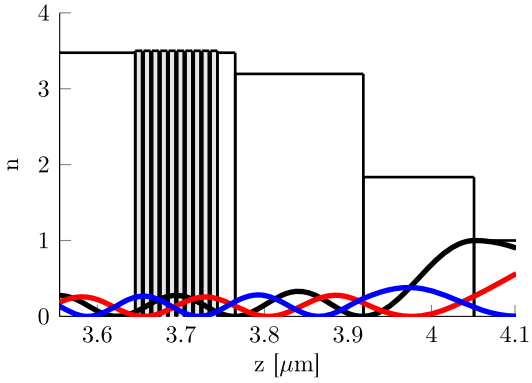

Fig. 1. Diagram of the material layers in the MQW structure. The vertical axis shows the refractive index of each material layer and the vertical grey lines represent the position of the QWs. The black, blue and red lines are standing waves at 980 nm, 930 nm, and 1030 nm, respectively, that have been rescaled for visibility. Not shown is a DBR on the left.

The QWs in the gain chip are optically pumped to have a carrier density that is high enough for them to provide sufficient optical gain over a wide spectral range, while the unexcited SESAM QW provides the saturable absorption. In all QWs, the carrier relaxation is modeled by specifying an initial carrier density at 300 K. The integration of the coupled Eqs. (1) and (2) determines the dynamic state of the QW carriers. The carriers in the inverted QWs are assumed to relax to a quasi-equilibrium distribution with the density given in the simulations using a relaxation time of 30 ps, while in the SESAM the quasi-equilibrium distribution has a density $5.0 \cdot 10^{14}$ m^{-2} and a relaxation time of 2 ps is chosen. The kinetic hole filling time is kept constant at a rate of 100 fs, which results in good agreement with full carrier scattering simulations [18]. The round trip time of a pulse in the cavity is 21 ps.

The simulations are performed by setting an initial background carrier density for the QWs such that the carriers in the QWs are inverted, and spontaneous emission starts to fill the cavity with photons. During each round trip the part of the field that experiences net gain will be amplified. Eventually a pulse will form in the cavity with a spectrum located within the spectral region of positive net gain. The pulse is amplified when passing through the gain chip and reduced when it passes through the SESAM. In this repeated process, the spectral and thus temporal pulse shape is dynamically optimized such that it extracts as much energy as possible from the gain chip, which is then balanced by the energy loss from the SESAM and the out coupling. Once the pulse shape has stabilized, the system is considered mode locked. In all our simulations, we verify the pulses to be mode locked by confirming that the pulse peak intensity and FWHM are constant over thousands of round trips. There are only three occasions when the system does not reach a mode-locked state: the background QW carrier density is too low, resulting in no net gain, and thus no pulse will ever form in the cavity; the background QW carrier density is too high, resulting in the formation of multiple pulses in the cavity; or the background QW carrier density is just below the onset of multiple pulse formation, resulting in a pulse with an oscillating amplitude or FWHM.

A. Short-Pulse Optimization

Our short-pulse optimization proceeds by first choosing the anti reflection coating on the gain chip such that the cavity has a flat and low GDD. Then, for a fixed cavity loss we adjust the carrier background density in the QWs to reduce the net gain in the cavity until a single mode-locked pulse solution is found. Finally, by performing a few more simulations, the output coupling and R_α are varied to check whether it is possible to further reduce the pulse FWHM. The last two steps are repeated until we are satisfied with the resulting mode-locked pulse. All computations are parallelized, optimized for speed, and run in parallel on an SGI UV2000 shared memory machine. A typical mode-locking simulation can easily take around 40 h.

The QW placement in the gain structure has been designed such that we avoid bleaching of the QW inversions, provide as broad as possible spectral amplification, have sufficiently high modal gain to overcome the cavity loss, suppress any microcavity effects, and finally reduce the influence of QW dispersion in the cavity. To accomplish all the above goals, the QWs of the MQW structure shown in Fig. 1 have been packed tightly around the first antinode of the standing wave at the peak gain wavelength. The standing waves of the DBR denoted in blue and red are resonant with QWs on either side of the antinode of the standing wave corresponding to the peak gain wavelength marked in black. Each QW will be in resonance with a standing wave of a different wavelength than the peak gain wavelength. This leads to an effectively inhomogeneous broadening of the total gain and thus, amplification of a wider spectral range compared to an RPG structure. As an additional desirable effect, the QWs have less influence on the GDD due to off resonant placements.

In the following simulation results, we are interested in adjusting the QW background carrier density to study the mode-locked pulse dynamics. The SESAM is fixed with a total absorption at 3.11% at 980 nm and the ratio of saturable absorption at 70%. In most of the shown results, the refractive index of the AR coating on top of the gain chip is fixed to the ideal value 1.72 to produce a flat GDD. The only exceptions are the narrow DBR simulations, where we adjust the refractive index to 1.86 to provide a similar GDD as the wide DBR simulation.

As the best example of our optimized simulation results, we show in Fig. 2 the final mode-locked pulse in the cavity and the QW inversion right after interaction with the pulse. With the wide DBR stopband and a QW background carrier density $n = 3.25 \cdot 10^{16}$ m^{-2}, the pulse has an intensity FWHM of 19 fs with a peak intensity 5.7 MW/cm^2. For the narrow DBR stopband and the QW background density of $n = 2.9 \cdot 10^{16}$ m^{-2}, the pulse intensity FWHM is 46 fs with a peak intensity 1.7 MW/cm^2. As mentioned above, a different AR coating is used for the narrow DBR stopband to make the GDD comparable to the GDD from the wide DBR simulation. Since this also amplifies the gain, we simultaneously reduce the QW carrier densities to allow for better comparison where the relevant difference between the two simulations is in the narrow stopband and slightly reduced carrier density.

In Fig. 2, the QW inversions are shown slightly after the passage of the 19 fs pulse, that is, at the time when the total number of carriers is at the lowest. The QWs that are placed furthest from the peak of the antinode in Fig. 1 are those with the most inverted carriers remaining after the pulse has passed. The four QWs that are placed closest to the peak of the antinode all have inversions that are nearly depleted by the cavity pulse. The inversion that remains is in the off resonant QWs or near the momentum value $\mathbf{k} = 0$, where there are fewer carriers. The instantaneous distributions are clearly distorted far from quasi-equilibrium distributions, and in addition, the placement of the QWs result in the

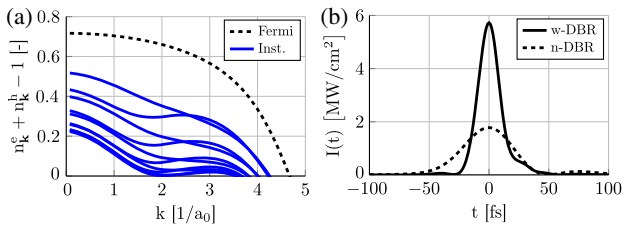

Fig. 2. Simultaneous snapshot of the mode-locked pulse and inversions in all the QWs. (a) Black dashed line is the inversion of the background Fermi distribution at a density $n = 3.25 \cdot 10^{16}$ m^{-2}, and each blue curve corresponds to the instantaneous inversion in separate QWs. (b) Solid (dashed) curve is the optimized mode-locked output pulse with intensity FWHM of 19 fs (46 fs) that results from using a wide (narrow) DBR stopband.

pulse interacting with each QW in a different way. The QWs that are closest to the peak of the antinode are also closest to resonance with the pulse, and thus their inversions are distorted the most.

To obtain further insights into the ultrashort pulse generation conditions, we look at the modal gain of the different QW configurations. Computationally, the modal gain can be found by comparing the spectrum of a low energy pulse before and after propagating through the structure. By simulating the full propagation through the material layers and interaction with the QWs, all dispersive effects are embedded in the spectrum of the pulse. By taking the modulus of the ratio of the two spectra, one finds the spectral amplification of the structure, and from looking at the phase, one is able to extract any dispersive effects from the QWs and the material layers. This makes it possible to calculate the gain spectrum at any QW carrier density.

Figure 3 shows both the spectral amplification of the MQW gain structure when compared to a traditional RPG structure and the GDD resulting from inverting the QWs in the two different QW arrangements. The QWs of the MQW structure are placed such that they are not in resonance with the wavelength corresponding to the peak gain. This reduces the spectral amplification from each QW, and thus, the QWs need a higher background carrier density in order for them to provide the same peak gain as the RPG structure. The placement of the QWs also means that the gain spectrum of the MQW structure is much broader than the gain from the RPG when they are compared at the same peak gain.

A careful GDD management strategy will take into account any linear dispersion when designing a chip for ultrashort pulse generation. However, the contribution from the electronic part of the QWs is dynamically dependent on the instantaneous carrier occupation numbers. In an experimental setup, the GDD is measured while the QWs are absorbing, and this provides some uncertainty on what influence the inverted QWs will have on the GDD [15]. Figure 3(b) shows the frequency-dependent GDD contribution from the inverted QWs relative to the absorbing QWs in both the MQW and RPG structures, clearly demonstrating how the optimized QW placement reduces the influence of the inverted carriers on the GDD.

B. Hysteresis Effects

We performed a series of simulations where we initialized the system from spontaneous emission and a positive net gain in the cavity. In Fig. 4, we show the resulting peak intensity and intensity FWHM of the mode-locked pulse as a function of the QW carrier densities. All mode-locked pulse results are stable for densities below $4.0 \cdot 10^{16}$ m^{-2}, where the net gain starts to

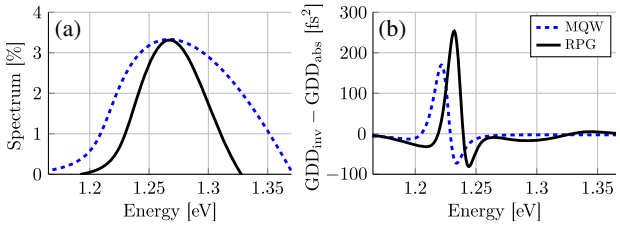

Fig. 3. Comparison of the modal gain and GDD at the carrier density $n = 3.25 \cdot 10^{16}$ m^{-2} ($2.22 \cdot 10^{16}$ m^{-2}) for the MQW (RPG) structure. (a) Modal gain of the two structures when they are clamped at the same peak gain. (b) Influence of inverted QWs on the GDD relative to absorbing QWs at a carrier density $n = 5.0 \cdot 10^{14}$ m^{-2}.

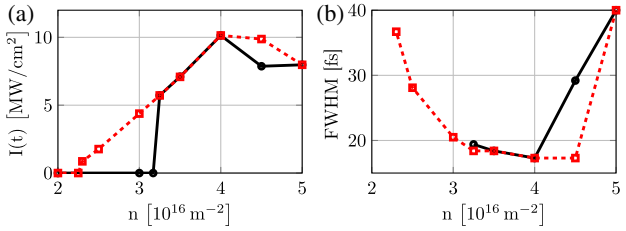

Fig. 4. Overview of the peak intensity and intensity FWHM of the mode-locked pulses that result from varying the initial QW background carrier density of the MQW structure. The solid black curves corresponds to simulation results that start from noise, and the dashed red curves are results that come from reducing the background density. (a) Peak pulse intensity. (b) Pulse intensity FWHM.

become too high and the pulses have more substructure or multiple pulses form in the cavity.

To check for the influence of non-equilibrium effects, we also performed a series of simulations where we begin from a mode-locked configuration and gradually reduce the carrier density. The points in Fig. 4 along the dashed red curves correspond to the peak intensity and intensity FWHM of the resulting mode-locked pulses, where the QW background carrier density has been reduced starting from $5.0 \cdot 10^{16}$ m^{-2}. Operationally, we reduced the QW background carrier density gradually, at a rate of $0.15 \cdot 10^{16}$ m^{-2} per ns.

As a surprising result, we find stable mode-locked pulses, even for carrier densities below $3.17 \cdot 10^{16}$ m^{-2} where the quasi-equilibrium modal gain in the cavity is less than the loss, and thus, no mode-locked pulses can appear from spontaneous emissions. The corresponding mode-locked pulse for each point along the red curve is verified to not change for tens of thousands of round trips. Only when we reach densities close to $2.25 \cdot 10^{16}$ m^{-2} is the mode-locked pulse no longer sustainable by the system and then gradually absorbed.

In Fig. 4(b), we observe that the MQW structure is able to take advantage of the increased carrier density to further reduce the pulse FWHM down to 17 fs. When the QW carrier density increases, some of the additional pulse energy is stored in a low amplitude tail; thus, the best compromise between the FWHM and a clean pulse is found near the density $3.25 \cdot 10^{16}$ m^{-2}.

Figure 5 shows the modal gain in the cavity at the time of initialization for select QW carrier densities. When the carrier density is too low there is no net gain in the cavity, as can be seen from the gain curve at the density $2.5 \cdot 10^{16}$ m^{-2}. When simulations with these densities are started from noise, the photons only see absorption in the cavity and thus will never grow to a mode-locked pulse. From the gain curve that corresponds to the carrier density $4.0 \cdot 10^{16}$ m^{-2}, it is noted that the MQW gain curves do not grow much in amplitude, but instead the gain is considerably broadened with increasing carrier density.

When the simulations are initialized from spontaneous emissions, the initial modal gain dictates the dynamic behavior. Thus, when there is less gain than loss in the cavity, there is no chance for net pulse amplification. However, if one starts from a previously mode-locked state and gradually reduces the background carrier density in the QWs, it is possible to end up in another mode-locked state. This state is not reachable by starting from spontaneous emissions, since the quasi-equilibrium gain is below the equilibrium absorption. One way to take advantage of this pure non-equilibrium phenomenon is the possibility to reduce

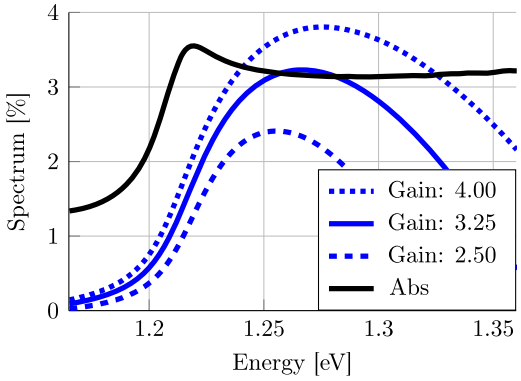

Fig. 5. Total cavity absorption in black and the modal gain of the MQW structure for select QW carrier densities.

the substructure of a mode-locked pulse, such as a low amplitude tail. For example, the trajectory of the red dashed line in Fig. 4(a) starts in a situation where there are multiple pulses developing in the cavity. When the QW carrier density is reduced to $3.25 \cdot 10^{16}$ m^{-2}, the FWHM of the pulse is 18 fs, slightly smaller than it would have been if starting from spontaneous emissions. The hysteresis effect has been observed in recent experiments by Waldburger *et al.* [24].

4. SUMMARY

In this paper, we have numerically designed schemes to generate ultrashort mode-locked pulses in special VECSEL configurations. We first minimize the cavity GDD over a wide range of wavelengths; this can be accomplished, for example, by using dispersion compensating layers. Next, the QWs of the gain chip are arranged to facilitate a short pulse. When placing QWs one has multiple goals such as: increased gain width, reduce bleaching of QW inversions, and the need for a high modal gain in order to overcome cavity loss.

As a result, we present an idealized MQW gain structure that has a wide amplification bandwidth and low dispersion, and it is capable of producing mode-locked pulses with a FWHM as short as 19 fs. As demonstrated here, during interaction with short pulses, the QW carrier distributions are significantly distorted from quasi-equilibrium Fermi distributions. Furthermore, we show how the non-equilibrium dynamics open up a whole new branch of mode-locked pulse solutions that are otherwise not accessible from just modal gain considerations.

Funding. Air Force Office of Scientific Research (AFOSR) (FA9550-14-1-0062).

Acknowledgment. This material is based upon work supported by the Air Force Office of Scientific Research under award number FA9550-14-1-0062.

REFERENCES

1. A. Garnache, S. Hoogland, A. C. Tropper, I. Sagnes, G. Saint-Girons, and J. S. Roberts, "Sub-500-fs soliton-like pulse in a passively mode-locked broadband surface-emitting laser with 100 mW average power," Appl. Phys. Lett. **80**, 3892 (2002).
2. U. Keller and A. C. Tropper, "Passively modelocked surface-emitting semiconductor lasers," Phys. Rep. **429**, 67–120 (2006).
3. A. H. Quarterman, K. G. Wilcox, V. Apostolopoulos, Z. Mihoubi, S. P. Elsmere, I. Farrer, D. A. Ritchie, and A. Tropper, "A passively mode-locked external-cavity semiconductor laser emitting 60-fs pulses," Nat. Photonics **3**, 729–731 (2009).
4. M. Hoffmann, O. D. Sieber, V. J. Wittwer, I. L. Krestnikov, D. A. Livshits, Y. Barbarin, T. Südmeyer, and U. Keller, "Femtosecond high-power quantum dot vertical external cavity surface emitting laser," Opt. Express **19**, 8108–8116 (2011).
5. A. Tropper, A. H. Quarterman, and K. G. Wilcox, "Ultrafast vertical-external-cavity surface-emitting semiconductor lasers," in *Semiconductors and Semimetals* (Elsevier, 2012), Vol. **86**.
6. B. Heinen, T.-L. Wang, M. Sparenberg, A. Weber, B. Kunert, J. Hader, S. W. Koch, J. V. Moloney, M. Koch, and W. Stolz, "106 W continuous-wave output power from vertical-external-cavity surface-emitting laser," Electron. Lett. **48**, 516–517 (2012).
7. T.-L. Wang, B. Heinen, J. Hader, C. Dineen, M. Sparenberg, A. Weber, B. Kunert, S. W. Koch, J. V. Moloney, M. Koch, and W. Stolz, "Quantum design strategy pushes high-power vertical-external-cavity surface-emitting lasers beyond 100 W," Laser Photon. Rev. **6**, L12–L14 (2012).
8. M. Scheller, T.-L. Wang, B. Kunert, W. Stolz, S. W. Koch, and J. V. Moloney, "Passively modelocked VECSEL emitting 682 fs pulses with 5.1 W of average output power," Electron. Lett. **48**, 588–589 (2012).
9. K. G. Wilcox, A. C. Tropper, H. E. Beere, D. A. Ritchie, B. Kunert, B. Heinen, and W. Stolz, "4.35 kW peak power femtosecond pulse mode-locked VECSEL for supercontinuum generation," Opt. Express **21**, 1599–1605 (2013).
10. C. Zaugg, Z. Sun, V. J. Wittwer, D. Popa, S. Milana, T. S. Kulmala, R. S. Sundaram, M. Mangold, O. D. Sieber, M. Golling, Y. Lee, J. H. Ahn, A. C. Ferrari, and U. Keller, "Ultrafast and widely tunable vertical-external-cavity surface-emitting laser, mode-locked by a graphene-integrated distributed Bragg reflector," Opt. Express **21**, 31548–31559 (2013).
11. S. Husaini and R. A. Bedford, Antiresonant Graphene Saturable Absorber Mirror for Mode-Locking VECSELs (personal communication, 2013).
12. K. Seger, N. Meiser, S. Y. Choi, B. H. Jung, D.-I. Yeom, F. Rotermund, O. Okhotnikov, F. Laurell, and V. Pasiskevicius, "Carbon nanotube mode-locked optically-pumped semiconductor disk laser," Opt. Express **21**, 17806–17813 (2013).
13. P. Klopp, U. Griebner, M. Zorn, and M. Weyers, "Pulse repetition rate up to 92 GHz or pulse duration shorter than 110 fs from a mode-locked semiconductor disk laser," Appl. Phys. Lett. **98**, 071103 (2011).
14. A. Laurian, C. Mart, J. Hader, J. V. Moloney, B. Kunert, and W. Stolz, "15 W Single frequency optically pumped semiconductor laser with sub-megaHertz linewidth," IEEE Photon. Technol. Lett. **26**, 131–133 (2014).
15. D. Waldburger, S. M. Link, M. Mangold, C. G. E. Alfieri, E. Gini, M. Golling, B. W. Tilma, and U. Keller, "High-power 100 fs semiconductor disk lasers," Optica **3**, 844–852 (2016).
16. O. D. Sieber, M. Hoffmann, V. J. Wittwer, M. Mangold, M. Golling, B. W. Tilma, T. Südmeyer, and U. Keller, "Experimentally verified pulse formation model for high-power femtosecond VECSELs," Appl. Phys. B **113**, 133–145 (2013).
17. H. Haug and S. W. Koch, *Quantum Theory of the Optical and Electronic Properties of Semiconductors*, 5th ed. (World Scientific, 2009).
18. I. Kilen, J. Hader, J. V. Moloney, and S. W. Koch, "Fully microscopic modeling of mode locking in microcavity lasers," J. Opt. Soc. Am. B **33**, 75–80 (2016).
19. J. Hader, S. W. Koch, and J. V. Moloney, "Microscopic theory of gain and spontaneous emission in GaInNAs laser material," Solid-State Electron. **47**, 513–521 (2003).
20. I. Kilen, J. Hader, J. V. Moloney, and S. W. Koch, "Ultrafast nonequilibrium carrier dynamics in semiconductor laser mode locking," Optica **1**, 192–197 (2014).
21. P. Klopp, U. Griebner, M. Zorn, A. Klehr, A. Liero, M. Weyers, and G. Erbert, "Mode-locked InGaAs-AlGaAs disk laser generating sub-200-fs pulses, pulse picking and amplification by a tapered diode amplifier," Opt. Express **17**, 10820–10834 (2009).
22. S. Backus, C. G. Durfee III, and M. M. Murnane, "High power ultrafast lasers," Rev. Sci. Instrum. **69**, 1207–1223 (1998).
23. S. J. Orfanidis, *Electromagnetic Waves and Antennas* (Rutgers University, 2008).
24. D. Waldburger, S. M. Link, C. G. Alfieri, M. Golling, and U. Keller, "High-power 100-fs SESAM-modelocked VECSEL," in *Lasers Congress 2016 (ASSL, LSC, LAC)* (Optical Society of America, 2016), paper. ATu1A.8.